S. S. BRIMZHANOVA[1, 2]*, A. A. AKHMADIYA[3,4], N. NABIYEV[3],
KH. MOLDAMURAT[4]

[1]*NPLC«A. Baitursynov Kostanay Regional University», Kostanay, Kazakhstan*
[2]*Kostanay Academy of the Ministry of Internal Affairs of the Republic of Kazakhstan named after Shrakbek Kabylbaev, Kostanay, Kazakhstan*
[3]*S.Seifullin Kazakh Agrotechnical University, Nur-Sultan, Kazakhstan*
[4]*L.N. Gumilyov Eurasian National University, Nur-Sultan, Kazakhstan*

DETERMINATION OF THE EARTHQUAKE EPICENTER USING THE MAXIMUM DISPLACEMENT METHOD OBTAINED BY SENTINEL-1A/B DATA VIA ESA SNAP SOFTWARE

This article discusses a method for determining an earthquake's epicenter using modern radar data from the Sentinel-1A/b remote sensing satellite. To determine the epicenter of the earthquake, finding the maximum displacement from the radar image data was used. The displacement (displacement) of the earth's crust was obtained by processing on the ESA SNAP software. Two earthquakes that occurred in 2020 were studied to determine the epicenters in the ascending and descending orbits of the satellite. These earthquakes occurred in Western Xizang, China, and Doganyol, Turkey. The maximum deviation from the epicenter's officially registered coordinates was 15.6 km for Doganyol and 3.2 km for the West Xinjiang Earthquake.

Keywords: Displacement, Radar image processing, Phase difference, artificial intelligence, Interferometric processing, Earthquake Epicenter.

Introduction. The concept of artificial intelligence and machine learning to help analysts do their jobs faster is discussed in the geospatial industry, but often only in the context of looking at a single image. What happens when an analyst receives up to fifteen images of the same area every day, while being responsible for monitoring several locations at once? When huge amounts of geospatial data arrive on a daily basis, even an entire team of analysts cannot scrutinize all the details. That's why artificial intelligence must become part of every analyst's workflow.

The deep learning capabilities of artificial neural networks allow them to be applied in various fields. In [1] the authors give an overview of deep learning methods of artificial neural networks and a brief review of works on the application of artificial neural networks in solving a number of applications, including the processing of remote sensing data obtained using unmanned aerial vehicles. In [2], a method for recognizing buildings on satellite images, based on the use of a fuzzy neural network for classification and the proposed set of informative features for constructing a rule base is presented. The best segmentation result has been obtained using a combined method consisting in the sequential application of the region growth method and fuzzy

C-means clustering. The application of fuzzy clustering reduces the number of regions and improves the quality of segmentation. It was revealed that in order to improve the quality of segmentation of satellite images it is advisable to perform morphological processing, which provides a reduction in the number of analyzed regions by merging segments and removing irrelevant fragments in terms of the considered problem. The average value of the number of correctly recognized buildings was 86%. Of particular interest is the possibility of applying ultra-precise neural networks based on the YOLO library to solve the problem of detection and recognition of objects using an unmanned aerial vehicle [3]. The authors argue that this algorithm can be used not only within the ground-based processing complex, but also on board an unmanned aerial vehicle, providing a real-time video information processing mode.

Interferometric processing of remote sensing radar data makes it possible to visually detect the earthquake epicenter from the phase image. The results of radar image processing show that the location of the epicenter is visible in the form of repeating linear spectra in the color palette of the phase image [4, 5]. The linear pattern, which has a rainbow pattern characteristic of an earthquake, it is concentrated in the epicenter zone in the form of concentric phase transitions, in the center of which as we can assume the center of the earthquake, and it is proportional to the earthquake magnitude. Radar remote sensing satellites Sentinel-1A/B launched since 2014 can be used to determine these earthquake epicenters [6, 7]. The main feature of these remote sensing data Sentinel-1A/B, first, they can be used to detect earthquake epicenter with greater coverage than others and second, they are free for end users. Monitoring of the same area can be repeated every 12 days with the same viewing geometry or angle. The epicenter of an earthquake is more easily detected than those caused by landslides and land subsidence [8-10]. The obtained radar images can be processed by special software such as ROI_PAC, GMTSAR, GAMMA, ENVI SARscape, ESA SNAP [11-14]. Some software is licensed for more than $10,000 and may not be available to the end user. On the contrary, ESA SNAP open source software developed by the European Space Agency and being in free access can be successfully used for earthquake epicenter determination [15]. In the future, we will use it to determine the location of the earthquake epicenter and develop an algorithm for the sequence of steps in the processing of Earth remote sensing radar data.

Data for the study. Two earthquakes are being studied. The first one was in Turkey near Doganjol on January 24, 2020. The second was in China, western Xinjiang the same year on July 22. They were with magnitudes M6.7 and 6.3. Sentinel-1 remote sensing radar data before- and after the earthquake were used to create a VV polarization phase difference with its topographic component subtracted (Figures 3-8). Sentinel-1A/B remote sensing radar data satellites operate at a wavelength of approximately 5.6 cm. Sentinel-1A and Sentinel-1B radar remote sensing data were used with ascending and descending orbits for two earthquakes (see Table 1). All these data were downloaded from https://scihub.copernicus.eu/. These data were obtained for the territory of Turkey and Western Xinjiang, which is shown in Fig.1, 2.

Table 1 – Satellite data

| №	Study area	Date	Orbit	Data from remote sensing radar satellites
1	China, Eastern Xinjiang	18.07.2020	Rising	S1A_IW_SLC__1SDV_20200718T121528_20200718T121555_033509_03E207_57A0
2		30.07.2020		S1A_IW_SLC__1SDV_20200730T121529_20200730T121556_033684_03E765_141D
3		14.07.2020	Descending	S1A_IW_SLC__1SDV_20200714T000951_20200714T001018_033443_03E012_72CA
4		28.07.2020		S1A_IW_SLC__1SDV_20200726T000952_20200726T001019_033618_03E572_17E0
5	Turkey, Doganjol	15.01.2020	Rising	S1A_IW_SLC__1SDV_20200115T152550_20200115T152618_030813_0388EA_9B20
6		27.01.2020		S1A_IW_SLC__1SDV_20200127T152550_20200127T152618_030988_038F14_4686
7		16.01.2020	Descending	S1A_IW_SLC__1SDV_20200116T032559_20200116T032627_030820_038928_F5DC
8		28.02.2020		S1A_IW_SLC__1SDV_20200128T032559_20200128T032627_030995_038F51_7D4F
9		21.01.2020	Rising	S1B_IW_SLC__1SDV_20200121T152522_20200121T152549_019917_025AC5_405C
0		02.02.2020		S1B_IW_SLC__1SDV_20200202T152522_20200202T152549_020092_02606E_C4D
1		22.01.2020	Descending	S1B_IW_SLC__1SDV_20200122T032514_20200122T032541_019924_025B00_46C6
2		03.02.2020		S1B_IW_SLC__1SDV_20200203T032513_20200203T032540_020099_0260A8_412D
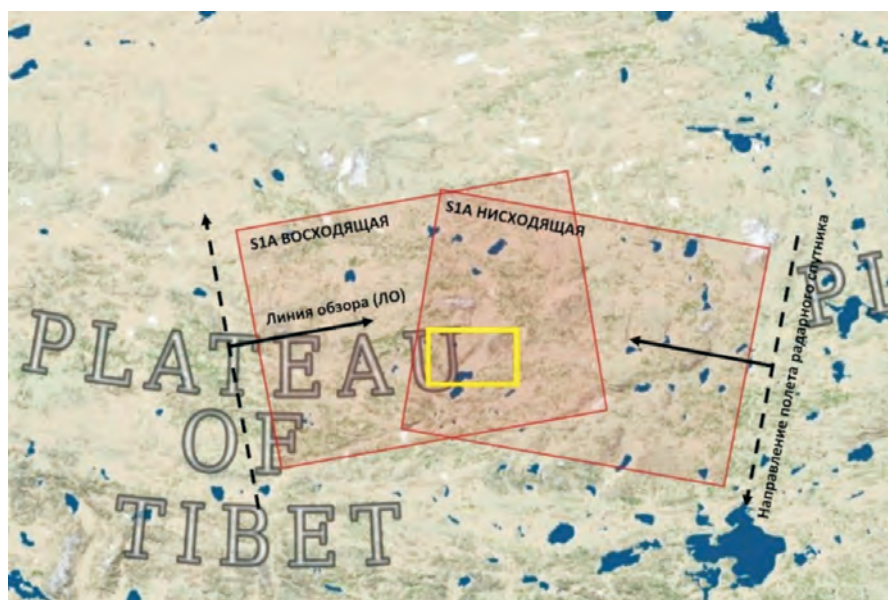
Figure 1 – Area of interest (yellow square outline) and trace of selected Sentinel-1A master scenes for both ascending and descending orbits. West Xizan, China.
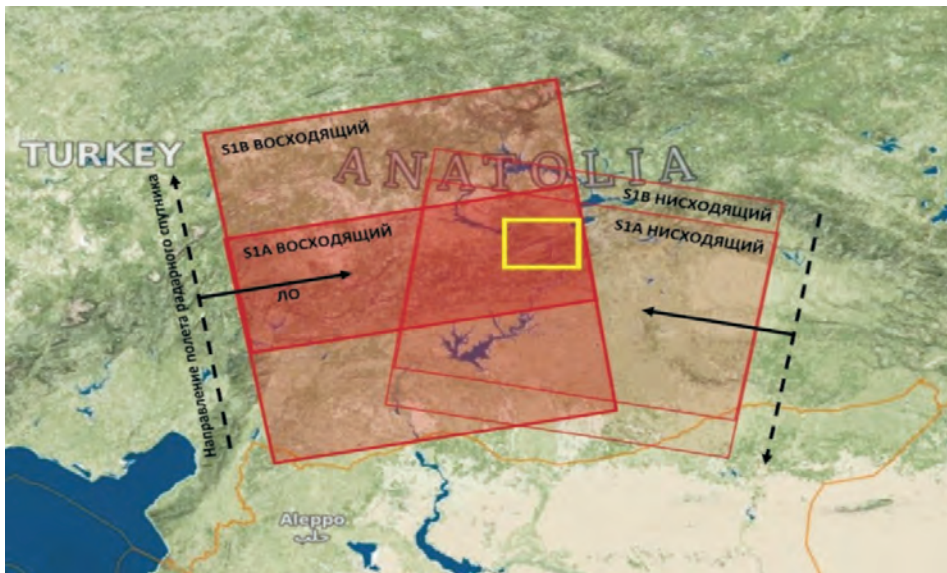
Figure 2 – Area of interest (yellow square outline) and trace of the selected master scenes of Sentinel-1A/B for both ascending and descending orbits. Doganjol, Turkey.
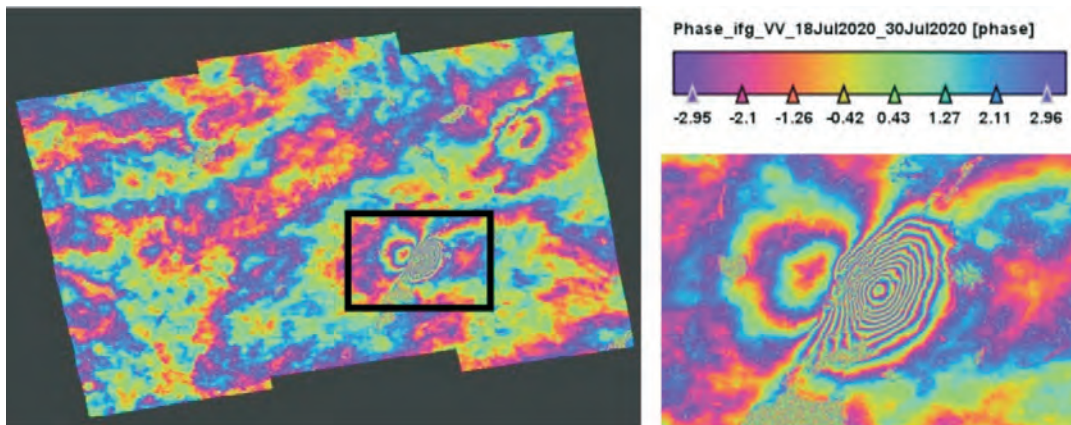

Figure 3 – Image of the phase difference of Sentinel-1A data for the earthquake in Western Xinjiang, China (ascending orbit).

Six interferometric pairs of Sentinel-1 data were obtained using ESA SNAP software (Figure 3-8):
1) the first pair of dates: July 18 and July 30, 2020.
2) Second pair of dates: July 14 and July 26, 2020.
3) Third pair of dates: January 15 and January 27, 2020.
4) Fourth pair of dates: January 16 and January 28, 2020.
5) Fifth pair of dates: January 21 and February 2, 2020.
6) Sixth pair of dates: January 22 and February 3, 2020.

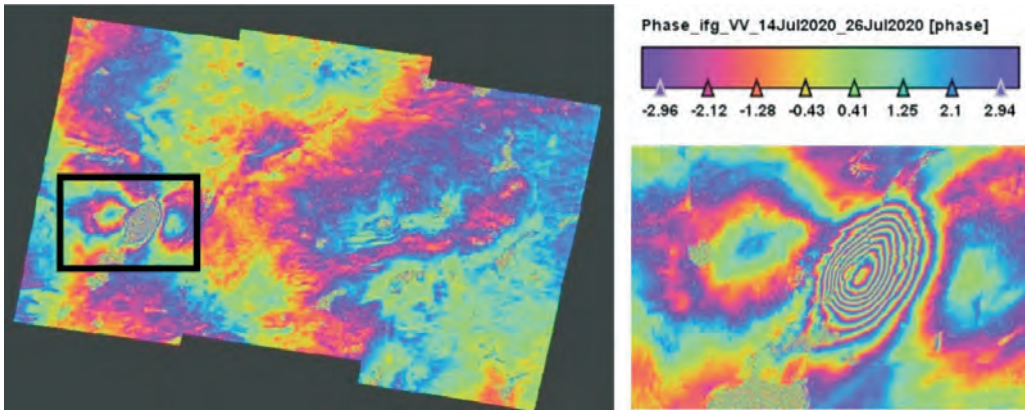*Figure 4* – Image of Sentinel-1A data phase difference for earthquake in Western Xinjiang, China (descending orbit).
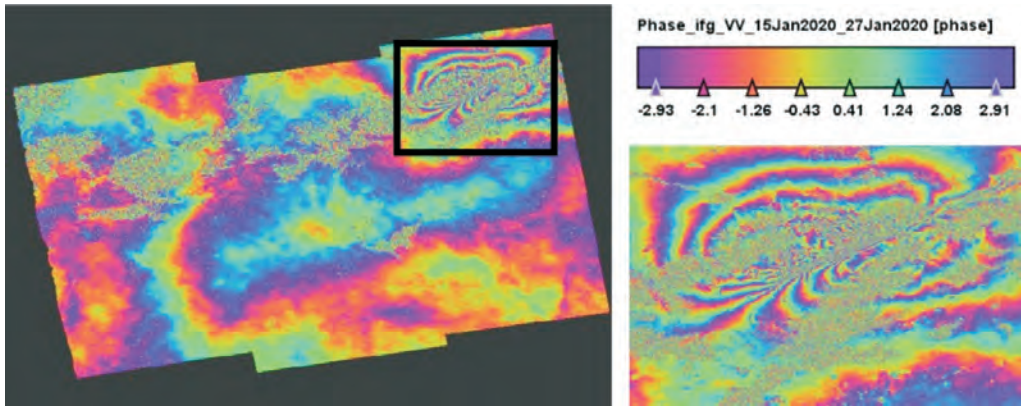

Figure 5 – Image of Sentinel-1A data phase difference for the earthquake in Doganjol, Turkey (ascending orbit).
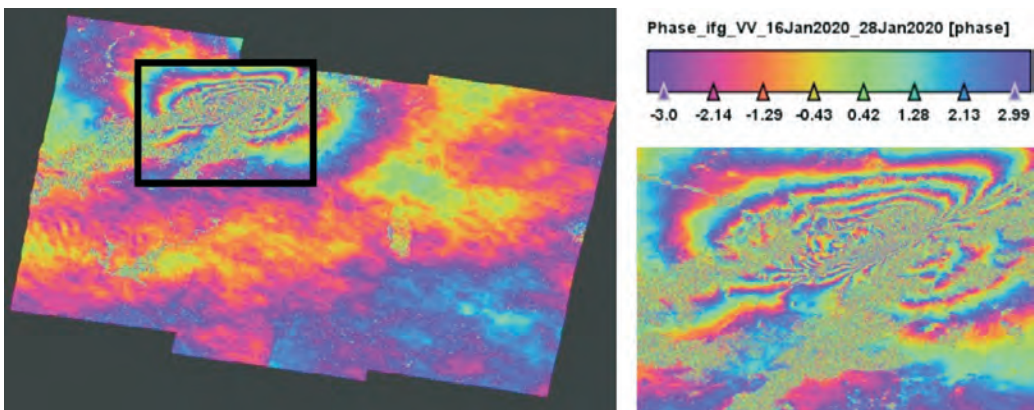

Figure 6 – Image of Sentinel-1A data phase difference for the earthquake in Doganjol, Turkey (descending orbit).
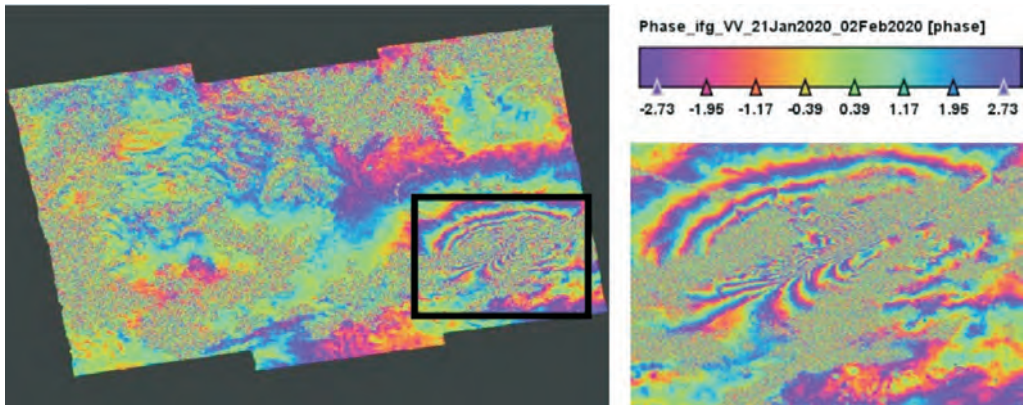
Figure 7 – Image of Sentinel-1B data phase difference for the earthquake in Doganjol, Turkey (ascending orbit).
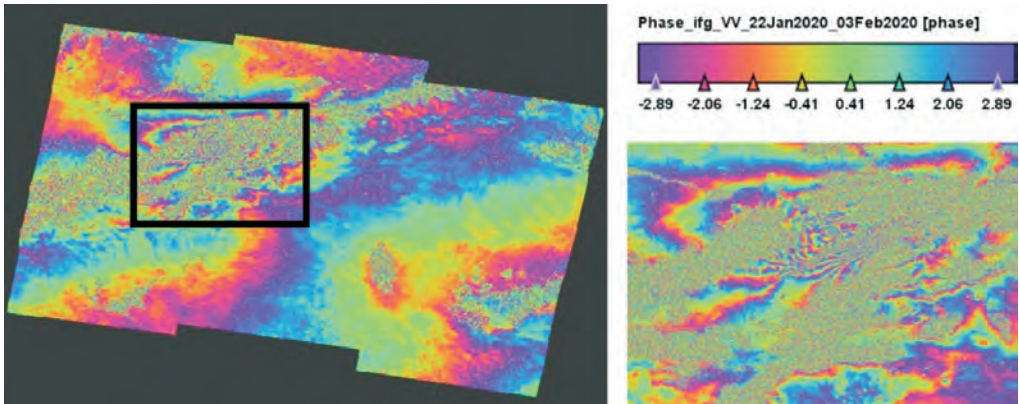

Figure 8 – Image of Sentinel-1B data phase difference for the earthquake in Doganjol, Turkey (descending orbit).

Radar image processing. Processing of radar images is performed using ESA SNAP software (see Fig. 9). Processing of radar images includes many steps, one of the important is the formation of the interferogram after the procedures of joint registration of each sub-band of Sentinel-1 data [16]. The output products of interferogram formation are difference-phase and coherent images. Phase difference is calculated as follows for each pixel for a pair of jointly registered radar images:

$$\Delta\varphi = \arctan\left(\frac{b_1}{a_1}\right) - \arctan\left(\frac{b_2}{a_2}\right) = \varphi_1 - \varphi_2$$

where a_1, a_2 are the real part of the complex number from a pair of radar images, and b_1, b_2 are the imaginary part of the complex number of each pixel of these radar images. The intensity or amplitude of the value is calculated from these parts of the complex number [17]:

$$A = \sqrt{a^2 + b^2}$$

The phase difference is the sum of several components associated with offset $\Delta\varphi_{defo}$, topographic phase related $\Delta\varphi_{topo}$, atmospheric phase delay $\Delta\varphi_{atmo}$ and noise $\Delta\varphi_{noise}$ effect [18]:

$$\Delta\varphi = \Delta\varphi_{defo} + \Delta\varphi_{topo} + \Delta\varphi_{atmo} + \Delta\varphi_{noise}$$

An earthquake causes a displacement of the earth's surface, where the phase associated with the displacement is much larger than the phase associated with the atmosphere and noise $\Delta\varphi_{defo} >> \Delta\varphi_{atmo} + \Delta\varphi_{noise}$. Knowing this, we can conclude that. The sum of atmospheric and noise phase effects is negligible compared to what is caused by the displacement from the earthquake. Therefore, the phase associated with the displacement is calculated as the subtraction of the topographic phase from the phase difference:

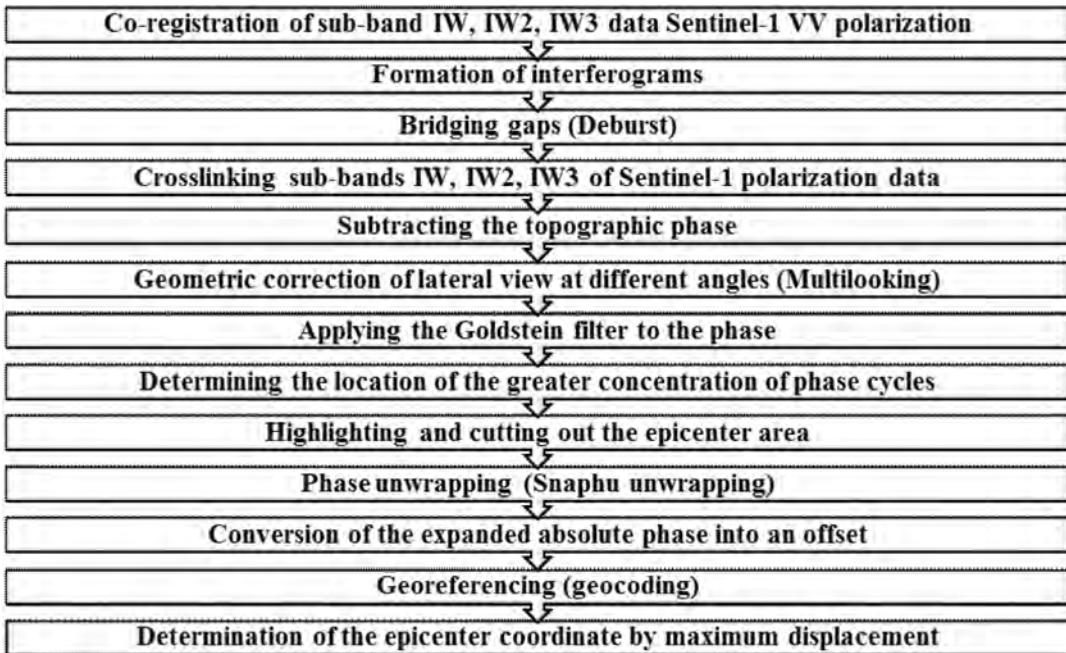$$\Delta\varphi_{defo} = \Delta\varphi - \Delta\varphi_{topo}$$

Co-registration of sub-band IW, IW2, IW3 data Sentinel-1 VV polarization
Formation of interferograms
Bridging gaps (Deburst)
Crosslinking sub-bands IW, IW2, IW3 of Sentinel-1 polarization data
Subtracting the topographic phase
Geometric correction of lateral view at different angles (Multilooking)
Applying the Goldstein filter to the phase
Determining the location of the greater concentration of phase cycles
Highlighting and cutting out the epicenter area
Phase unwrapping (Snaphu unwrapping)
Conversion of the expanded absolute phase into an offset
Georeferencing (geocoding)
Determination of the epicenter coordinate by maximum displacement

Figure 9 – Block diagram of radar images processing
for earthquake epicenter detection

The topographic phase subtraction is used to calculate the phase associated with the displacement when processing radar images. The topographic phase depends on the spatial baseline $B_\perp$ [19] (see Fig. 10). The topographic phase is calculated as follows:

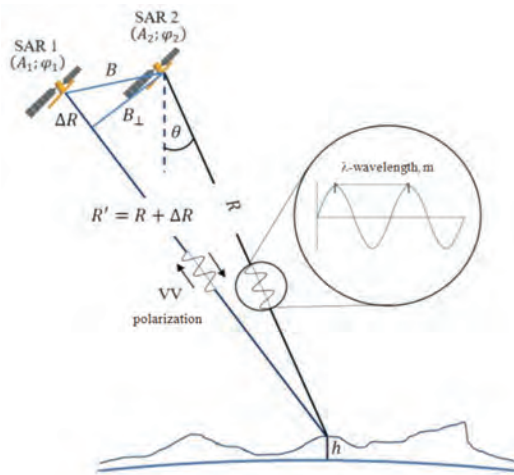$$\Delta\varphi_{topo} = \frac{4\pi}{\lambda} \cdot \frac{B_\perp}{R\sin(\theta)} h$$

Figure 10 – Application of Sentinel-1A/B remote sensing radar satellites for phase
difference imaging from data before earthquake (SAR 1) and after earthquake (SAR 2)

The topographic phase subtraction procedure is performed using a digital elevation model (DEM) and a phase difference image. The DEM image contains the value of elevation h. DEM image is used to calculate the topographic phase component $\Delta\varphi_{topo}$ [20-22].

The phase associated with the offset can be distorted by noise. Noise can arise from temporal decorrelation, geometric decorrelation, volumetric scattering, and processing error. A Goldstein filter is used to eliminate or partially reduce the effect of phase noise [23-27].

Approximate determination of the earthquake epicenter location begins after the Goldstein filter. The location of the earthquake epicenter can be seen in the filtered displacement-related phase images as a rainbow pattern periodically repeated in the color palette, their concentration consisting of a large number of phase transitions from -π to +π (see Figure 11).

The displacement associated with the West Xinjiang earthquake can be estimated using the phase profile between «O» and «9» (a distance of 10 km) in Figure 11. Here the number of phase transitions k on the linear profile is 9. If we multiply this number by the Sentinel-1 wavelength (λ=5.6 cm), we can find the displacement relative to the line of sight:

$$d_{los} = k\lambda = 9 \times 5,6 \approx 50 \text{ см}$$

Two radar images before and after an earthquake with the same geometric perspective (view) are sufficient to detect the earthquake epicenter by displacement. Using ESA SNAP software, the absolute phase image is converted into a displacement image. Before this, it is necessary to perform a phase sweep, i.e. the calculation of the absolute phase of the image, which is performed by a script developed by Chen and Zebker [28-30]. This script is written in C and must be executed separately in the ESA SNAP software.
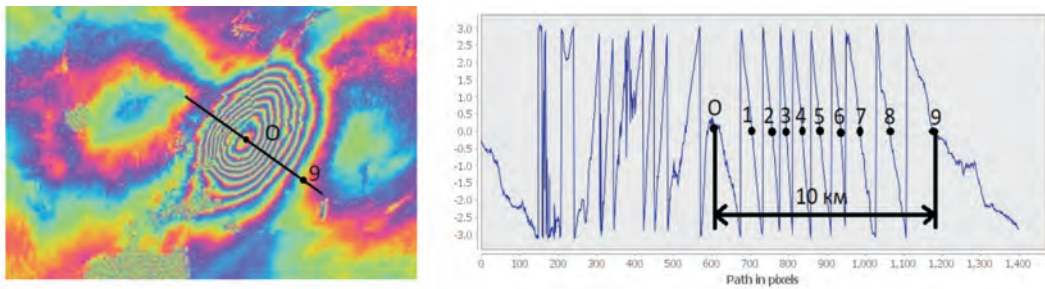
Figure 11 – Phase image associated with the displacement (top) and phase profile (bottom). Earthquake in Western Xinjiang in 2020. The phase image was created from Sentinel-1A data for July 14 and 26.

The maximum displacement coordinate is determined using a geocoded displacement image. The epicenter of the earthquake is clearly visible in the displacement image. If the color palette or maximum threshold is chosen correctly, it stands out well in the processed radar image (see Figure 12).
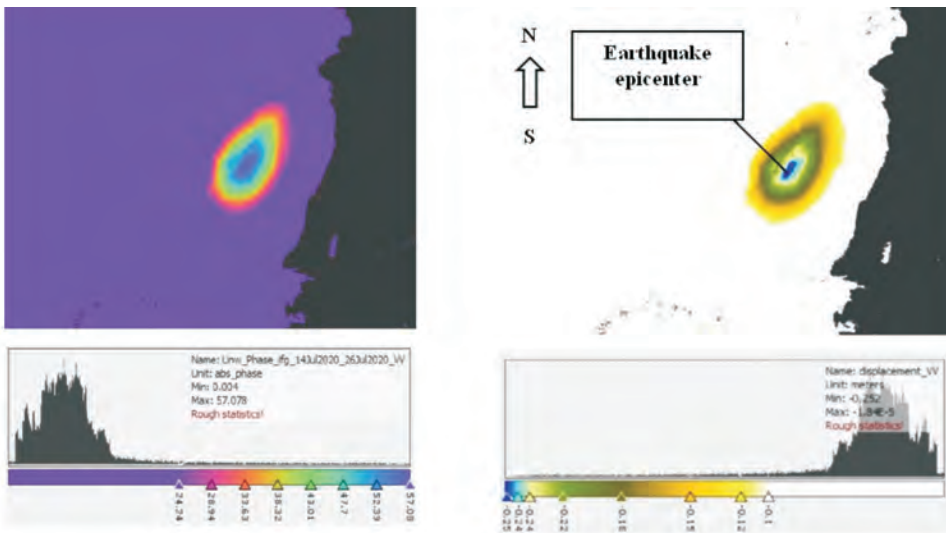

Figure 12 – Expanded phase image (left) and earthquake-induced crustal displacement (right) in Western Xinjiang with different color palettes.

The absolute phase of the expanded phase image has a maximum value of 57.078 in Fig. 12. If the threshold value is greater than 24.24, the epicenter becomes clearly visible in the color palette of the expanded phase image on the left side of Fig. 12. The maximum value of the absolute phase $\varphi_{abs}^{\max}$ consists of the number of phase cycles N, which is calculated as follows:

$$N = \frac{\varphi_{abs}^{\max}}{2\pi} = \frac{57,078}{6,283} = 9,08$$

The number of phase cycles is approximately equal to the number of phase transitions λ, which is shown in Fig. 11. The maximum value of the offset deviation associated with an earthquake is 0,252 meters. If the threshold value is greater than 0,1 m, the epicenter becomes visible in the displacement image color palette on the right side of Fig. 12.

Results. To determine the epicenter of the earthquake, different images of both the rising and falling orbits of Sentinel-1A/B were obtained. See Figure 13-15. The baseline of each interferometric pair of radar images is shown in Table 2.

Table 2 – Evaluation of the baseline

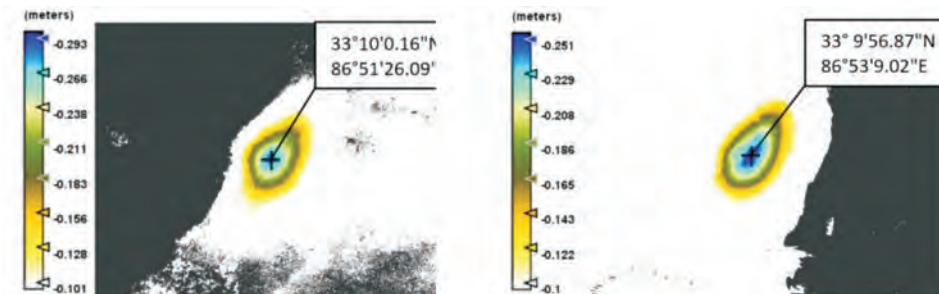| №	Research area	Orbit	Before earthquake date	After the earthquake date	Baseline B, meters
1	Western Xinjiang, China	ascending	18.07.2020	30.07.2020	110,411
2		descending	14.07.2020	26.07.2020	122,695
3	Doganjol, Turkey	ascending	15.01.2020	27.01.2020	21,374
4		descending	16.01.2020	28.01.2020	76,907
5		ascending	21.01.2020	02.02.2020	58,858
6		descending	22.01.2020	03.02.2020	39,15

Figure 13 – offset images to determine the epicenter of the West Sizzan earthquake with coordinates. Left: Sentinel-1A with ascending orbit from dates July 18 and 30, 2020. Right: with a downward orbit from dates July 14 and 26, 2020.

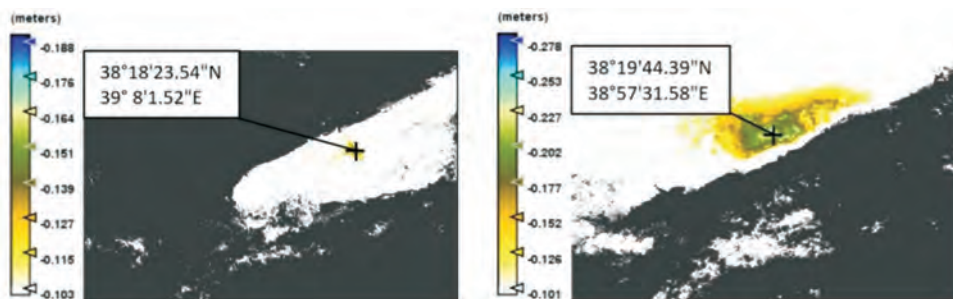*Figure 14* – Images of displacements to determine the epicenter of the Doganyol earthquake with coordinates. Left: Sentinel-1A with ascending orbit from dates 15 and 27 January 2020. Right: with a downward orbit from dates January 16 and 28, 2020.
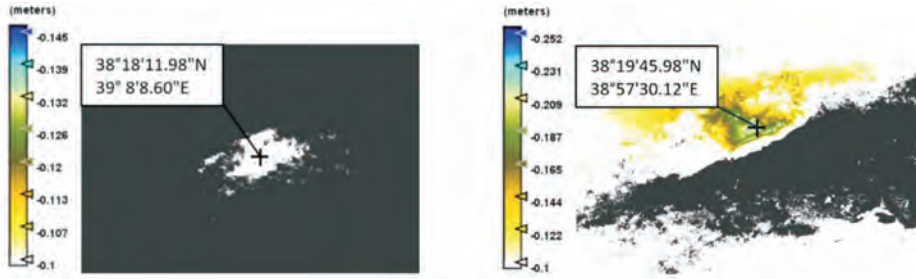
Figure 15 – Images of displacements to determine the epicenter of the Doganyol earthquake with coordinates. Left: Sentinel-1B with ascending orbit from dates January 21 and February 2, 2020. Right: with a downward orbit from dates January 22 and February 3, 2020.

Accuracy of determination of epicenters of earthquakes was carried out according to official data of the USA Geological Survey using a priori information about epicenter coordinates. Western Xinjiang: 33.144°N 86.864°E; Doganol: 38.431°N 39.061°E. Distances between official epicenter of this earthquake and data received after processing of Sentinel-1A/B RS radar data are shown in table 3 and on fig.16. Distances between nearest epicenters S1A and S1B with ascending and descending orbits equal 0,4 and 0,03 km for Doganyol earthquake.

Table 3 – Accuracy of determination of earthquake epicenters

№	Research area	Orbit	Before earthquake date	After the earthquake date	Deviation from official data, distance
1	Western Xinjiang, China	S1A ascending	18.07.2020	30.07.2020	2.38 km
2		S1A descending	14.07.2020	26.07.2020	3.2 km
3	Doganyol, Turkey	S1A ascending	15.01.2020	27.01.2020	15.2 km
4		S1A descending	16.01.2020	28.01.2020	14.4 km
5		S1A ascending	21.01.2020	02.02.2020	15.6 km
6		S1A descending	22.01.2020	03.02.2020	14.37 km

Note: S1A - Sentinel-1A, S1B - Sentinel-1B remote sensing radar satellites
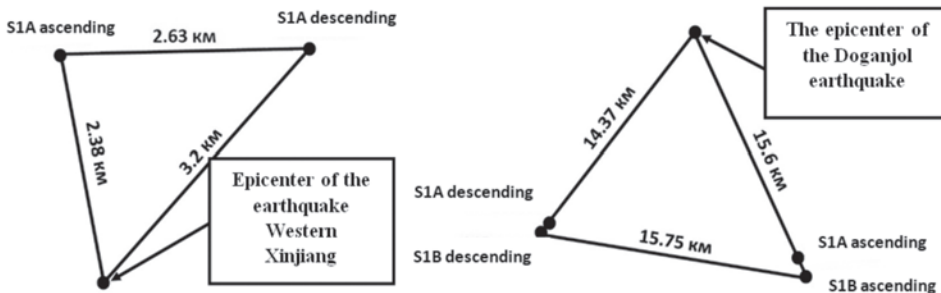

Figure 16 – Distance between official and received earthquake epicenters for western Xinjiang and Doganol with ascending (asc) and descending (desc) orbits of Sentinel-1A/B satellites

Conclusion. Sentinel-1A/B radar remote sensing data are applicable to determine the epicenter of the earthquake. The maximum error of distance deviation from the official one is 15.6 km for the Doganyol earthquake. The distance between descending orbits for the Doganyol earthquake is up to 0.4 km. The same geometric survey with ascending or descending orbits shows the minimum distance between the obtained epicenters. A different geometric view with different orbits (ascending and descending) leads to a larger deviation of the distance error. The case of the Doganhol earthquake, we have volumetric scattering from vegetation; therefore, the phase goes with more noise than in the Xinjiang case. The western Xinjiang case has a distance error of 3.2 km, which is better than the Doganol case, probably this is because of the large baseline of 110-120 meters.

Determining the location of the earthquake epicenter associated with displacement can be found by the maximum value (in centimeters) of displacement pixels in the obtained image. This method will be referred to as determining the earthquake epicenter from the maximum displacement. The displacement threshold value was chosen to be 10 cm. This value indicates that more than this value the pixels will refer to the earthquake zone in the displacement image.

The next step is to improve the algorithm for automatically extracting the maximum offset value from the interferometric pair of Sentinel-1A/B radar images using ESA SNAP software. It takes a long time to process the radar images to create the offset images and extract their maximum value. The execution time depends on the quality of the phase image as it is distorted by noise due to temporal decorrelation and seasonal changes during snaphu-unwrapping processing. Shaphu-unwrapping for a complete Sentinel-1 scene can take one day. Fast automatic processing of radar images requires a supercomputer with large RAM. That's because the original Sentinel-1 data takes up 14 gigabytes of data, and it can grow several times due to intermediate data during processing. We can use the Graph Builder tool in ESA SNAP software to automate radar image processing in the future.

REFERENCES

1 A. Carrio, C. Sampedro, A. Rodriguez-Ramos, P. Campoy. "A review of deep learning methods and applications for unmanned aerial vehicles", Journal of Sensors, 2017.

2 S. V. Naderan. "Automated building extraction system applied on high resolution satellite imagery using fuzzy neural network", Int. J. Information Content and Processing, 1:2 (2015), pp. 188–193 (in Russian).

3 N. Tijtgat, Wiebe Van Ranst, B. Volckaert, T. Goedeme, Filip De Turck. "Embedded real-time object detection for a UAV warning system", Proceedings of 2017 IEEE International Conference on Computer Vision Workshops (ICCVW) (Venice, Italy, October 22-29, 2017), 2018, pp. 2110–2118.

4 E. J. Fielding et al., «Surface Deformation Related to the 2019 M-w 7.1 and 6.4 Ridgecrest Earthquakes in California from GPS, SAR Interferometry, and SAR Pixel Offsets,» Seismological Research Letters, vol. 91, no. 4, pp. 2035-2046, Jul 2020, doi: 10.1785/0220190302.

5 Z. C. Huang, G. H. Zhang, X. J. Shan, W. Y. Gong, Y. F. Zhang, and Y. C. Li, «Co-Seismic Deformation and Fault Slip Model of the 2017 Mw 7.3 Darbandikhan, Iran-Iraq Earthquake Inferred from D-InSAR Measurements,» Remote Sensing, vol. 11, no. 21, Nov 2019, Art no. 2521, doi: 10.3390/rs11212521.

6 S. Plank, «Rapid Damage Assessment by Means of Multi-Temporal SAR - A Comprehensive Review and Outlook to Sentinel-1,» Remote Sensing, vol. 6, no. 6, pp. 4870-4906, Jun 2014, doi: 10.3390/rs6064870.

7 S. Wang, Y. Zhang, Y. Wang, J. Jiao, Z. Ji, and M. Han, «Post-seismic deformation mechanism of the July 2015MW 6.5 Pishan earthquake revealed by Sentinel-1A InSAR observation,» Scientific reports, vol. 10, no. 1, pp. 18536-18536, 2020 Oct 2020, doi: 10.1038/s41598-020-75278-0.

8 M. LazeckY et al., «Displacements Monitoring over Czechia by IT4S1 System for Automatised Interferometric Measurements Using Sentinel-1 Data,» Remote Sensing, vol. 12, no. 18, Sep 2020, Art no. 2960, doi: 10.3390/rs12182960.

9 T. Gatsios, F. Cigna, D. Tapete, V. Sakkas, K. Pavlou, and I. Parcharidis, «Copernicus Sentinel-1 MT-InSAR, GNSS and Seismic Monitoring of Deformation Patterns and Trends at the Methana Volcano, Greece,» Applied Sciences-Basel, vol. 10, no. 18, Sep 2020, Art no. 6445, doi: 10.3390/app10186445.

10 X. H. Xu, D. T. Sandwell, and B. Smith-Konter, «Coseismic Displacements and Surface Fractures from Sentinel-1 InSAR: 2019 Ridgecrest Earthquakes,» Seismological Research Letters, vol. 91, no. 4, pp. 1979-1985, Jul 2020, doi: 10.1785/0220190275.

11 S. H. Yun, H. Zebker, P. Segall, A. Hooper, and M. Poland, «Interferogram formation in the presence of complex and large deformation,» Geophysical Research Letters, vol. 34, no. 12, Jun 2007, Art no. L12305, doi: 10.1029/2007gl029745.

12 D. Suresh and K. Yarrakula, «InSAR based deformation mapping of earthquake using Sentinel 1A imagery,» Geocarto International, vol. 35, no. 5, pp. 559-568, Apr 2020, doi: 10.1080/10106049.2018.1544289.

13 H. Cui and X. J. Zha, «Parallel Image Registration Implementations for GMTSAR Package,» Seismological Research Letters, vol. 89, no. 3, pp. 1129-1136, May-Jun 2018, doi: 10.1785/0220170171.

14 B. Zhang, J. Y. Li, and H. R. Ren, «Using Phase Unwrapping Methods to Apply D-InSAR in Mining Areas,» Canadian Journal of Remote Sensing, vol. 45, no. 2, pp. 225-233, Mar 2019, doi: 10.1080/07038992.2019.1583097.

15 J. M. D. Blasco, M. Foumelis, C. Stewart, and A. Hooper, «Measuring Urban Subsidence in the Rome Metropolitan Area (Italy) with Sentinel-1 SNAP-StaMPS Persistent Scatterer Interferometry,» Remote Sensing, vol. 11, no. 2, Jan 2019, Art no. 129, doi: 10.3390/rs11020129.

16 B. Wieczorek, «EVALUATION OF DEFORMATIONS IN THE URBAN AREA OF OLSZTYN USING SENTINEL-1 SAR INTERFEROMETRY,» Acta Geodynamica Et Geomaterialia, vol. 17, no. 1, pp. 5-18, 2020, doi: 10.13168/agg.2019.0041.

17 J. S. Lee, K. W. Hoppel, S. A. Mango, and A. R. Miller, «INTENSITY AND PHASE STATISTICS OF MULTILOOK POLARIMETRIC AND INTERFEROMETRIC SAR IMAGERY,» Ieee Transactions on Geoscience and Remote Sensing, vol. 32, no. 5, pp. 1017-1028, Sep 1994, doi: 10.1109/36.312890.

18 S. Devaraj and K. Yarrakula, «Assessment of topographical and atmospheric errors in Sentinel 1 derived DInSAR,» Geocarto International, doi: 10.1080/10106049.2020.1822926.

19 Y. J. Zhang, H. Fattahi, and F. Amelung, «Small baseline InSAR time series analysis: Unwrapping error correction and noise reduction,» Computers & Geosciences, vol. 133, Dec 2019, Art no. 104331, doi: 10.1016/j.cageo.2019.104331.

20 Y. T. Dong, H. J. Jiang, L. Zhang, and M. S. Liao, «An Efficient Maximum Likelihood Estimation Approach of Multi-Baseline SAR Interferometry for Refined Topographic Mapping in Mountainous Areas,» Remote Sensing, vol. 10, no. 3, Mar 2018, Art no. 454, doi: 10.3390/rs10030454.

21 T. Zeng, M. Zhu, C. Hu, W. M. Tian, and T. Long, «Experimental Results and Algorithm Analysis of DEM Generation Using Bistatic SAR Interferometry With Stationary Receiver,» Ieee Transactions on Geoscience and Remote Sensing, vol. 53, no. 11, pp. 5835-5852, Nov 2015, doi: 10.1109/tgrs.2015.2422303.

22 Q. Sun, L. Zhang, J. Hu, X. L. Ding, Z. W. Li, and J. J. Zhu, «Characterizing sudden geo-hazards in mountainous areas by D-InSAR with an enhancement of topographic error correction,» Natural Hazards, vol. 75, no. 3, pp. 2343-2356, Feb 2015, doi: 10.1007/s11069-014-1431-x.

23 C. Danisor and A. Pepe, «Comparative study of SAR interferometric phase filtering algorithms,» in Advanced Topics in Optoelectronics, Microelectronics, and Nanotechnologies Ix, vol. 10977, M. Vladescu, R. Tamas, and I. Cristea Eds., (Proceedings of SPIE, 2018.

24 A. Tripathi and S. Kumar, Effect of Phase Filtering on Interferometry based Displacement Analysis of Cultural Heritage Sites (2018 5th Ieee Uttar Pradesh Section International Conference on Electrical, Electronics and Computer Engineering). 2018, pp. 18-22.

25 Q. Q. Feng, H. P. Xu, Z. F. Wu, Y. A. You, W. Liu, and S. Q. Ge, «Improved Goldstein Interferogram Filter Based on Local Fringe Frequency Estimation,» Sensors, vol. 16, no. 11, Nov 2016, Art no. 1976, doi: 10.3390/s16111976.

26 A. Mestre-Quereda, J. M. Lopez-Sanchez, J. Selva, and P. J. Gonzalez, «An Improved Phase Filter for Differential SAR Interferometry Based on an Iterative Method,» Ieee Transactions on Geoscience and Remote Sensing, vol. 56, no. 8, pp. 4477-4491, Aug 2018, doi: 10.1109/tgrs.2018.2820725.

27 Z. Y. Suo, J. Q. Zhang, M. Li, Q. J. Zhang, and C. Fang, «Improved InSAR Phase Noise Filter in Frequency Domain,» Ieee Transactions on Geoscience and Remote Sensing, vol. 54, no. 2, pp. 1185-1195, Feb 2016, doi: 10.1109/tgrs.2015.2476355.

28 C. W. Chen and H. A. Zebker, «Network approaches to two-dimensional phase unwrapping: intractability and two new algorithms,» Journal of the Optical Society of America a-Optics Image Science and Vision, vol. 17, no. 3, pp. 401-414, Mar 2000, doi: 10.1364/josaa.17.000401.

29 C. W. Chen and H. A. Zebker, «Phase unwrapping for large SAR interferograms: Statistical segmentation and generalized network models,» Ieee Transactions on Geoscience and Remote Sensing, vol. 40, no. 8, pp. 1709-1719, Aug 2002, doi: 10.1109/tgrs.2002.802453.

30 C. W. Chen and H. A. Zebker, «Two-dimensional phase unwrapping with use of statistical models for cost functions in nonlinear optimization,» Journal of the Optical Society of America a-Optics Image Science and Vision, vol. 18, no. 2, pp. 338-351, Feb 2001, doi: 10.1364/josaa.18.000338.

С. С. БРИМЖАНОВА[1,2], А. А. АХМАДИЯ[3,4], Н. К. НАБИЕВ[3], Х. МОЛДАМУРАТ[4]

[1]*«А. Байтұрсынов атындағы Қостанай өңірлік университеті» КЕАҚ, Қостанай, Қазақстан*
[2]*Шырақбек Қабылбаев атындағы ҚР ІІМ Қостанай академиясы, Қостанай, Қазақстан*
[3]*С. Сейфуллин атындағы Қазақ Агротехникалық Университет, Нұр-Сұлтан, Қазахстан*
[4]*Л.Н. Гумилев атындағы Еуразия Ұлттық Университеті, Нұр-Сұлтан, Қазахстан*

ESA SNAP БАҒДАРЛАМАЛЫҚ ҚАМТАМАСЫЗДАНДЫРУДЫ ҚОЛДАНА ОТЫРЫП SENTINEL-1A/B МӘЛІМЕТТЕРІНЕН АЛЫНҒАН МАКСИМАЛДЫ ЫҒЫСУ ӘДІСІ БОЙЫНША ЖЕР СІЛКІНІСІНІҢ ЭПИЦЕНТРІН АНЫҚТАУ

Бұл мақалада Sentinel-1A/B Жерді қашықтықтан зондтау спутнигінің заманауи радарлық деректерін қолдана отырып, жер сілкінісінің эпицентрін анықтау әдісі қарастырылады. Жер

қыртысының ығысу (орын ауыстыру) көрінісі ESA SNAP бағдарламалық жасақтамасында өңдеу арқылы алынды. 2020 жылы болған екі жер сілкінісі спутниктің жоғары және төмен орбиталары арқылы эпицентрлерді анықтау дәлдігі зерттелді. Бұл жер сілкіністері Батыс Шыңжаңда, Қытайда және Доганьолда, Түркияда болды. Эпицентрдің ресми тіркелген координатынан максималды ауытқуы Доганьол үшін 15.6 км және Батыс Шыңжаңда жер сілкінісі үшін 3.2 км болды.

Түйін сөздер: орын ауыстыру, радар суреттерін өңдеу, фаза айырмасы, жасанды интеллект, интерференциялық өңдеу, жер сілкінісінің эпицентрі.

С. С. БРИМЖАНОВА[1, 2], А. А. АХМАДИЯ[3, 4], Н. К. НАБИЕВ[3], Х. МОЛДАМУРАТ[4]

[1]*НАО «КРУ имени А.Байтурсынова», Костанай, Казахстан*
[2]*Костанайская академия МВД РК имени Шыракбека Кабылбаева, Костанай, Казахстан*
[3] *Казахский Агротехнический Университет им. С. Сейфуллина, Нур-Султан, Казахстан*
[4] *Евразийский Национальный Университет им. Л. Н. Гумилева, Нур-Султан, Казахстан*

ОПРЕДЕЛЕНИЕ ЭПИЦЕНТРА ЗЕМЛЕТРЯСЕНИЯ ПО МЕТОДУ МАКСИМАЛЬНОГО СМЕЩЕНИЯ, ПОЛУЧЕННОГО ПО ДАННЫМ SENTINEL-1A/B С ИСПОЛЬЗОВАНИЕМ ПРОГРАММНОГО ОБЕСПЕЧЕНИЯ ESA SNAP

В данной статье рассматривается методика определения эпицентра землетрясения с использованием современных радарных данных спутника дистанционного зондирования Земли Sentinel-1A/B. Методы интеллектуального анализа, поиска и распознавания целевых объектов на данных дистанционного зондирования Земли большого объема. Для определения эпицентра землетрясения использовался метод нахождения максимального смещения по данным радиолокационного изображения. Картины смещения (перемещения) земной коры были получены обработкой на программном обеспечении ESA SNAP. Два землетрясения, которые произошли в 2020 году были изучены на предмет точности определения эпицентров по восходящей и нисходящей орбитам спутника. Эти землетрясения имели место в Западном Синьцзяне, Китае и Доганьоле, Турция. Максимальное отклонение от официально зарегистрированной координаты эпицентра составило 15.6 км для Доганьола и 3.2 км для Западно-Синьцзянского землетрясения.

Ключевые слова: смещение, обработка радарных изображений, разность фазы, искусственный интеллект, интерферометрическая обработка, эпицентр землетрясения.